corrosion and materials degradation

MDPI

Article

Investigating the Fatigue Response of Cathodically Charged Cold-Finished Mild Steel to Varied Hydrogen Concentrations

Emmanuel Sey and Zoheir N. Farhat *

Department of Mechanical Engineering, Dalhousie University, Halifax, NS B3H 4R2, Canada; em445321@dal.ca
* Correspondence: zoheir.farhat@dal.ca

Abstract: This study investigates the fatigue behavior of cold-finished mild steel subjected to electrochemical hydrogen charging under controlled conditions. Samples were subjected to hydrogen charging at constant time in a fixed electrolyte pH, after which the samples underwent fatigue testing under constant loading condition with fixed frequency. The primary objective was to assess the impact of varying hydrogen permeation levels on the number of cycles to failure. The experimental results revealed a complex relationship between hydrogen concentration and fatigue life. Initially, as hydrogen permeation increased, the number of cycles to failure substantially decreased, demonstrating the detrimental effect of diffused hydrogen on the fatigue resistance of samples. This decline in fatigue life was attributed to hydrogen embrittlement (HE) and hydrogen-enhanced decohesion (HEDE) phenomena, which collectively facilitate crack initiation and propagation. However, at high hydrogen concentrations, an unexpected increase in the number of cycles to failure was observed suggesting the existence of a threshold hydrogen concentration beyond which the fatigue mechanisms may be altered, potentially due to a saturation of hydrogen-related defects and mechanisms such as hydrogen-enhanced localized plasticity (HELP). The discovery from this research has significant implications for the material's application in hydrogen-rich environments, such as those encountered in the energy and transportation industries.

Keywords: cathodic charging; cyclic loading; hydrogen embrittlement; diffusible hydrogen

Citation: Sey, E.; Farhat, Z.N. Investigating the Fatigue Response of Cathodically Charged Cold-Finished Mild Steel to Varied Hydrogen Concentrations. *Corros. Mater. Degrad.* **2024**, *5*, 406–426. https://doi.org/10.3390/cmd5030018

Academic Editor: Huixing Li

Received: 10 August 2024
Revised: 30 August 2024
Accepted: 6 September 2024
Published: 9 September 2024

1. Introduction

Hydrogen embrittlement (HE) arises when hydrogen atoms permeate into a metal, often during exposure to hydrogen-rich environments in processes such as operational exposure in scenarios such as high-pressure hydrogen storage, acidic, or alkaline conditions. This infiltration of hydrogen can destabilize the metal through several mechanisms: it diminishes the cohesive forces between metal atoms (a phenomenon known as decohesion) [1,2], facilitating the initiation and propagation of cracks. Additionally, certain metals, notably titanium and zirconium, may react with hydrogen to form brittle metal hydrides [3], enhancing their susceptibility to cracking. Furthermore, diffused hydrogen can induce localized slipping within the metal's crystal structure, triggering premature failure under stress.

Fatigue failure occurs when a material progressively weakens and ultimately fractures under repeated cycles of stress levels below the material's ultimate tensile strength [4,5]. This failure initiates at stress concentrators such as notches, holes, or surface imperfections, where cracks start to form and subsequently extend with each load cycle. The propagation rate of these cracks hinges on the applied stress range [6,7], such as alternating tension and compression, and the properties of the material [8–10], including chemical composition, microstructure (grains arrangement and size), fracture toughness, and hardness. Eventually, the crack reaches a critical size, rendering the remaining cross-sectional area inadequate to bear the load, which leads to a sudden material fracture with little to no forewarning. HE and fatigue failure, though distinct phenomena, are closely interlinked and can significantly

compromise the structural integrity and lifespan of metallic components, particularly in high-stress engineering environments. The interaction between these two processes is crucial for understanding their combined impact on material failure.

The presence of hydrogen notably accelerates fatigue failure in metals [11], primarily through reduction of the energy required to initiate microcracks. Hydrogen intensifies the rate of crack propagation during each fatigue cycle as it promotes localized plasticity [12] and reduces the fracture toughness of the material at the crack tip. This leads to accelerated crack growth under cyclic loading. HE also lowers the threshold stress intensity factor for crack growth [13,14], allowing cracks to extend at lower stress intensities than those observed in non-embrittled metals. Consequently, hydrogen presence significantly diminishes the fatigue life of a component, with cracks forming sooner and extending more rapidly.

In a study examining the impact of diffusible hydrogen on the fatigue life of spot welds in high-tensile-strength steel sheets [15], researchers found that both the number of cycles to failure and the endurance limit decreased as the diffusible hydrogen content increased at a constant amplitude-loading frequency. This phenomenon was attributed to the accumulation of hydrogen and its influence on crack growth behavior, facilitated by two primary mechanisms: hydrogen-enhanced local plasticity (HELP) and hydrogen-enhanced strain-induced vacancies (HESIV).

The HELP mechanism reveals how hydrogen contributes to the localized increase in plastic deformation around stress concentrators [16,17], which can lead to the early onset of material failure. On the other hand, the HESIV mechanism focuses on how hydrogen affects the metal's microstructural properties [17]. Specifically, it emphasizes the interaction between hydrogen and the vacancies that arise from irregularities in dislocation movement during plastic deformation. This interaction leads to an increased concentration of vacancies, which significantly impacts the metal's mechanical properties. These vacancies may coalesce into microvoids or facilitate the nucleation of microcracks. Under cyclic loading, these microvoids and microcracks are prone to expansion, resulting in premature material failure.

Another comprehensive study conducted on the fatigue crack growth characteristics of electron-beam-melted Ti-6Al-4V alloy in a high-pressure hydrogen environment demonstrated a notably faster fatigue crack growth rate [18] compared to that observed in air. This escalated rate of crack propagation was attributed to several hydrogen-related mechanisms that intensify the fatigue behavior of this titanium alloy. The primary mechanism cited by the researchers is HELP [19], which suggests that the presence of hydrogen facilitates increased localized plastic deformation at the crack tip. This deformation accelerates the crack growth under cyclic loading conditions. Additionally, the study referenced the adsorption-induced dislocation emission (AIDE) mechanism [20], which involves hydrogen atoms reducing the energy barrier for dislocation emission at the crack tip. This process enhances the mobility of dislocations, contributing to the rapid expansion of the crack.

Furthermore, hydrogen-enhanced decohesion (HEDE) [2] was identified as a critical factor influencing the alloy's fatigue performance. This mechanism proposes that hydrogen atoms weaken the metallic bonds within the material's lattice structure, particularly around the crack tip, thereby promoting the separation of the lattice and facilitating crack extension. These findings were thoroughly contextualized in a review by Lynch [20], which provides a detailed analysis of these mechanisms.

Given the synergistic effects between hydrogen embrittlement and fatigue failure, it is imperative for engineers to consider both factors when designing and selecting materials for applications likely to encounter hydrogen exposure or where high-cycle fatigue is anticipated. This dual consideration is essential to enhance safety and reliability in such applications.

In the transition toward sustainable energy systems and the reduction of carbon emissions, the co-firing of hydrogen (H2) with natural gas emerges as a critical technology for cleaner power generation [21–24]. Hydrogen can significantly contribute to this transition by displacing gaseous fossil fuels, as its combustion produces fewer greenhouse gases

(GHGs). The blending of hydrogen with natural gas, however, may lead to HE under static and cyclic stresses, which necessitates the need to investigate this phenomenon.

Numerous studies have examined the HE behaviors of various materials under hydrogenated conditions. However, there is a need for further research on other mechanical properties of these materials, as information on some aspects remains scarce. In particular, there is limited data on the fatigue behavior of materials concerning the hydrogen concentration. Given the critical areas of application of low-carbon steel, which may experience cyclic loading during service in the presence of a hydrogen environment, such as oil and gas pipelines and pressure vessels due to pressure changes, it is imperative to study how low-carbon steel responds to hydrogen permeation and diffusion under fatigue loading.

This study aims to assess the impact of varying hydrogen concentrations on the fatigue life of cold-finished mild steel, establish the hydrogen concentration threshold above which fatigue performance significantly deteriorates, investigate the microstructural damage in mild steel subjected to different hydrogen concentrations and their correlation with fatigue properties, and explore the fundamental mechanisms of hydrogen embrittlement under cyclic loading conditions and their contribution to fatigue failure.

2. Experimental Protocols

2.1. Material

Standardized cold-finished mild steel (AISI 1018) coupons with dimensions as shown in Figure 1 were used. Samples were carefully machined to ensure smooth, flat surfaces and uniform dimensions.

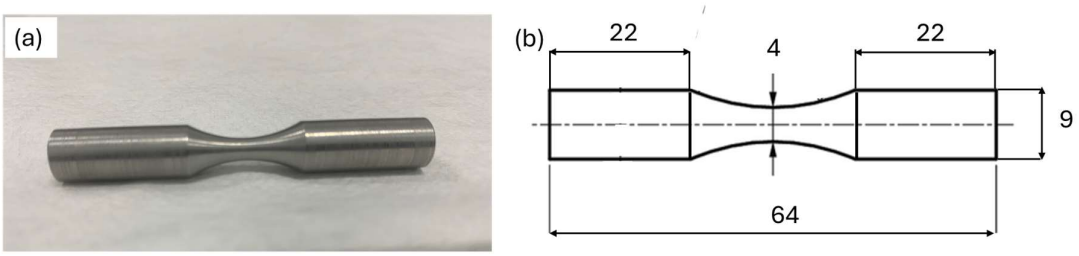

Figure 1. (**a**) Definite image of test specimen. (**b**) Illustrative diagram of specimen's dimensions (mm).

To verify the uniqueness of the properties of the acquired samples presumed to be cold-finished mild steel for this study, various characterization techniques were employed to provide comprehensive information on the chemical composition, microstructure, and crystalline structure.

Inductively coupled plasma mass spectrometry (ICP-MS) was utilized to determine the chemical composition of the test samples. This technique operates by dissolving and ionizing the samples, followed by measuring the mass-to-charge ratio of the ions present. The resulting data provided precise elemental composition details of the samples as given in Table 1 below.

Table 1. Chemical compositional outcome from ICP analysis.

Element	Fe	C	Mn	Si	S	Cu	Ni	Cr
Composition (wt%)	98.14	0.14	0.47	0.25	0.004	0.08	0.04	0.07

Scanning electron microscopy (SEM) was employed to analyze the microstructure, surface morphology, and metallographic features of the samples as given in standards [25,26]. The sample preparation involved sectioning and mounting in Bakelite resin, followed by grinding with progressively finer grit papers (240, 320, 400, 600, and 800) to remove sectioning scratches and achieve a smooth surface. To obtain a mirror-like, oxidation-free surface essential for effective microstructural examination, the sample was further polished using 1-micron and 0.3-micron alumina suspensions on an emery cloth. The polished

samples were then etched with Nital to reveal the microstructure before being examined under SEM.

While steel is generally known to have a body-centered cubic (BCC) structure, X-ray diffraction (XRD) analysis was performed to verify the crystalline structure of the test samples. The sample was prepared to meet the specifications required by the Bruker D8 Advanced X-ray diffraction system. The Bragg angle range of scanning was set from 20 to 100 degrees with 0.0490 step size. The diffraction pattern obtained was analyzed using EVA software equipped with an XRD system to identify the crystalline phases present in the samples.

The hardness of the samples was determined using the Rockwell hardness testing technique according to standards [27,28] with scale B. The sample surface was prepared to be smooth and free of contaminants that could affect the test results. The sample was then securely positioned on the testing platform of the Rockwell hardness tester. A 1/16-inch steel ball indenter was brought into contact with the sample surface, and a minor load of 10 kgf was applied to create an initial indentation, allowing the indenter to seat properly on the surface. Once the minor load was stabilized, a major load of 100 kgf was applied, resulting in deeper penetration of the indenter into the sample. The depth of the indentation was automatically measured by the equipment after holding the major load for a specified dwell time.

In a preceding study on the tensile behavior [29] of similar samples, mechanical properties such as yield strength, ultimate tensile strength, and toughness were determined by subjecting the samples to uniaxial tensile testing. Plots of stress against strain were generated, with a 0.2% offset calculated to determine the yield strength, which was found to be ~650 MPa.

2.2. Electrochemical/Cathodic Charging and Electrolyte

Hydrogen content of the steel was determined using a double electrolyte technique developed by Devanathan and Stachurski [30], in accordance with ISO 17081 [31] and outlined in our previous work [32].

A thin steel specimen was first polished and cleaned and then clamped in the permeation cell between the charging and oxidation cells, serving as the working electrode. Both the oxidation and charging cells utilized 0.1 M NaOH as the electrolyte (pH 12.5). However, a recombination poison, ammonium thiocyanate (NH4SCN), was added to the charging cell to prevent hydrogen atoms from recombining into H_2. The oxidation cell was equipped with an electrochemical workstation to monitor and measure the oxidation current generated as hydrogen atoms permeated through the specimen and reached the oxidation side's surface. In the charging cell, a power supply unit (PSU) had its positive terminal attached to a platinum counter electrode (anode) and its negative terminal connected to the steel specimen (cathode). An applied constant current controlled the quantity of hydrogen ions generated. In accordance with ISO 17081 [31], the permeation test provided values for effective diffusivity (D_{eff}), hydrogen concentration in interstitial lattice and reversible trap sites (C_H), and time to steady state (t_{ss}) for the sample, as shown in Table 2.

Table 2. Results from permeation tests.

	Current Density (mA/cm^2)	D_{eff} (m^2/s)	C_H (mol/m^3)	t_{ss} (min)
Material	10	3.38×10^{-11}	3.14	120

Based on the permeation experiments, the concentration of hydrogen dissolved in the steel can be quantified for different charging currents using Sieverts' law (Equation (1)) [33–35], where the constant factor *K* was calculated for the specimen using the charging current density

and corresponding hydrogen concentration. This constant was then used to correlate various hydrogen concentrations with charging current densities, as summarized in Table 3.

$$C_H = K\sqrt{i} \quad (1)$$

where C_H denotes the hydrogen concentration, K, a constant, and i, the current density.

Table 3. Selected electrochemical hydrogen charging parameters from permeation test results.

Hydrogen Content (wppm)	Current Density (mA/cm^2)	Charging Time (min)
0.00	0.00	0
0.05	0.16	180
0.20	2.49	
0.40	9.99	
0.60	22.49	
0.80	39.99	
1.00	62.48	
1.40	122.47	
1.60	159.96	
1.80	202.45	
2.00	249.93	

In this study, fatigue specimens were subjected to an electrochemical hydrogen charging process (Figure 2). The setup included a charging cell containing the electrolyte (0.1 M NaOH) and sample, a 1-ampere potentiostat to ensure consistent and controlled hydrogen charging, and a data entry and collection system. Based on the results of the preceding permeation tests, 11 samples were selected and tested under varying hydrogenating conditions, as given in Table 3 below. The same electrolyte as the permeation experiment with a pH of 12.5 and 3.3 g/L NH_4SCN was used. In this setup, the samples served as the working electrode, while platinum was used as the counter electrode. The charging cell was purged with argon gas to remove oxygen and mitigate its impact on the process. To ensure full hydrogen saturation, charging was conducted for 180 min, equivalent to 1.5 times the steady-state time (t_{ss}) determined from the permeation tests. The samples were immersed in the electrolyte such that the narrow (gauge) area was fully in contact with the electrolyte, ensuring uniform exposure and effective hydrogen diffusion, as evidenced by bubbling during the process. The amount of hydrogen diffused into each sample during the charging process was subtly estimated based on the charging current, as mentioned above.

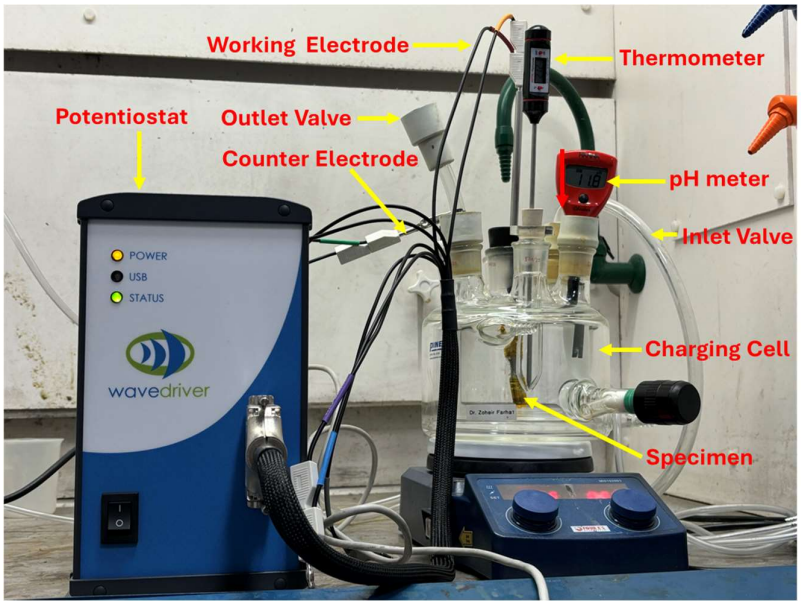

Figure 2. Electrochemical hydrogen charging set-up.

2.3. Fatigue Testing

Immediately after cathodic charging, each sample was tested under cyclic loading with constant but alternating tensile and compressive loads (Figure 3) on the top and bottom surfaces of the samples, respectively. The load, which was applied at the free end, was calculated based on 50% of material's yield strength, known from the preceding experiment with respect to the standard bending equations for the specimen as a circular cross-section cantilever, given in Equation (2) below. Cyclic loading on samples was done using TecQuiment's rotating fatigue machine (SM1090V-Nottingham, UK). This equipment functions based on Wohler's test [36,37]. Samples were subjected to cantilever loading, as shown in Figure 4. It has a main unit and a separate control and instrumentation unit (Figures 5 and 6).

$$\sigma = \frac{lF \times 32}{\pi D^3} \tag{2}$$

where l is the distance from the midpoint of the sample to the end where the load is applied, F is the applied load, D is the minimum neck area diameter, and σ is the applied stress.

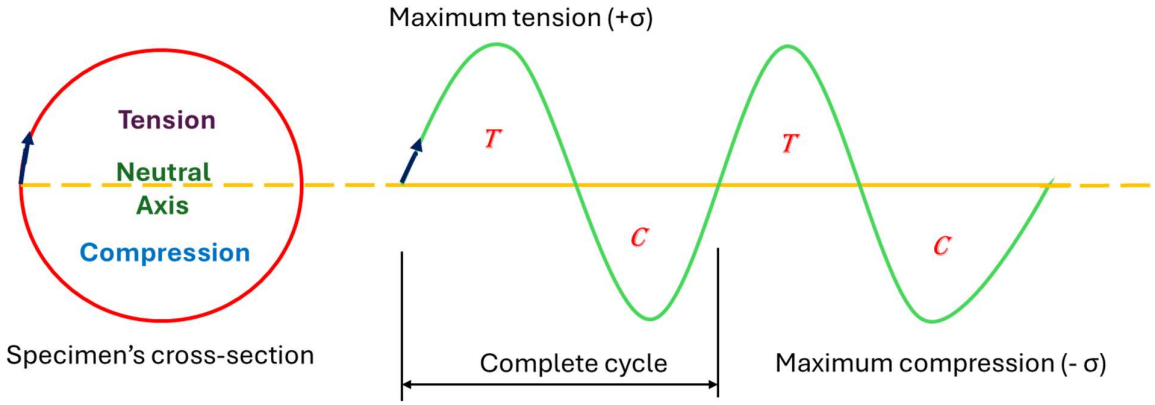

Figure 3. Schematic representation of specimen cyclic loading mechanism.

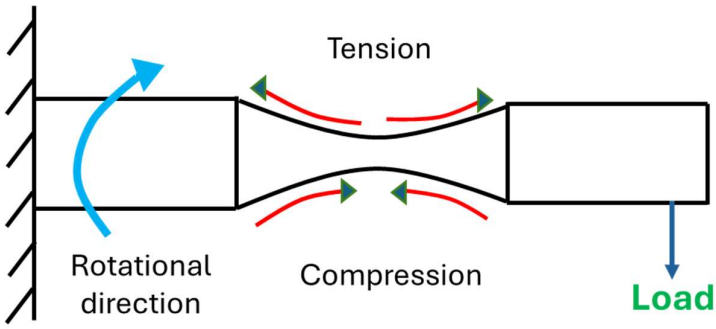

Figure 4. Graphical illustration of rotating cantilever loading of specimen.

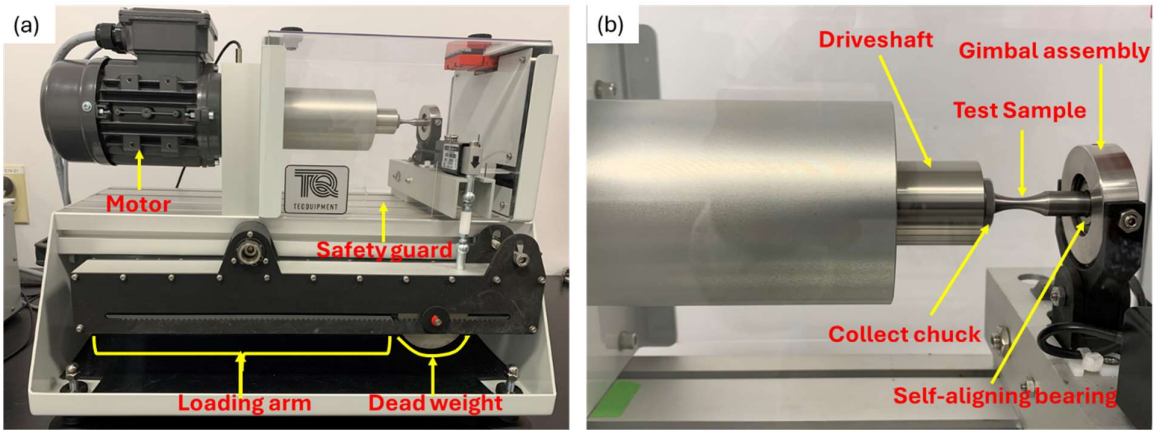

Figure 5. Main unit of fatigue testing set-up; (**a**) Overview of main unit showing major components; (**b**) Close-up view of specimen loading position and rotation mechanisms.

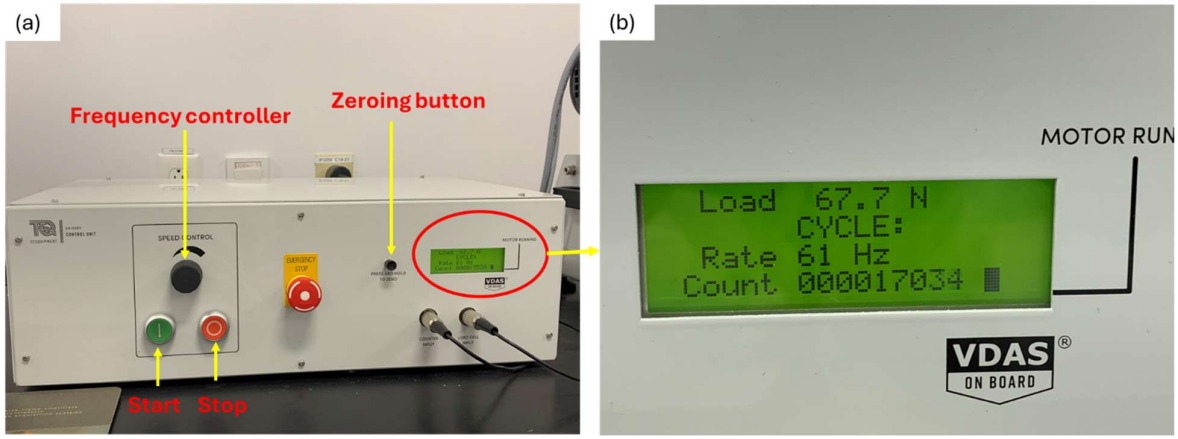

Figure 6. Control and instrumentation unit; (**a**) Parts of the control and instrumentation unit; (**b**) Magnified view of circled area in (**a**).

The main unit rotates the sample under an applied constant load, as its motor turns a coupling and driveshaft, which turns a collect chuck. The chuck grips the end of the test sample with uniform pressure around its circumference. The gimbal assembly houses a self-aligning bearing, which rotates together with the free end of the test specimen (Figure 5a,b). Counting of the number of cycles (rotations) and the measurement of the applied load are respectively done by an embedded sensor and a load cell. It is also equipped with a safeguard cover which stops the test automatically when opened.

The instrumentation unit allows the control of the rotating speed of the specimen (Figure 6a,b). It also displays the applied testing conditions, frequency and load as well as the instantaneous number of cycles.

A constant frequency of 60 Hz was applied for all samples; hence, the exposure of samples to cyclic loading remained unchanged, implying that any changes in fatigue behavior were primarily due to changes in material properties rather than external loading conditions.

3. Results and Discussion

3.1. Microstructure

The X-ray diffraction (XRD) analysis conducted on samples revealed a matching pattern of peaks with the characteristic peaks defined in the powder diffraction file (PDF) number, as given in Figure 7. This matching pattern indicates that the major constituent of the samples is alpha ferrite, having a body-centered cubic (BCC) crystal structure as expected. Its presence as the major constituent hints that the samples have a microstructure predominantly composed of ferrite.

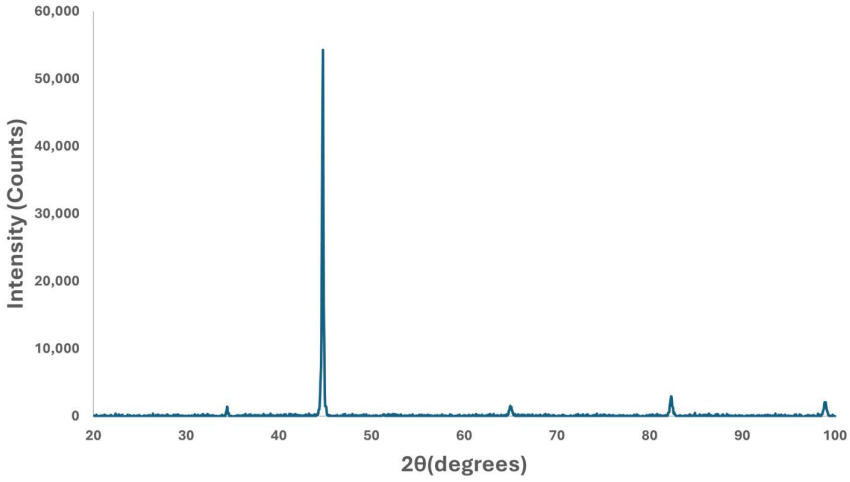

Figure 7. X-ray diffraction pattern of specimen.

The Rockwell hardness test conducted on the cold-finished mild steel sample resulted in a hardness value of 91.91 HRB. The obtained hardness value is relatively high as compared to fully annealed mild steel, which is typically in the range of 70 to 85 HRB [38], indicating substantial work hardening due to the cold-finishing process of these samples. The cold-finishing process refines the grain structure and increases the dislocation density within the steel resulting in work hardening, which significantly increases the material's hardness.

The metallographic analysis conducted under SEM revealed a microstructural composition characterized by homogeneous distribution of distinct pearlite and ferrite grains (Figure 8). The average ferrite grain size is about 15 μm, while pearlite is only 3 μm

In addition to the grain structure, the SEM images also show the presence of inclusions within the material. Inclusions are foreign particles or impurities that are trapped within the grains or at the grain boundaries. These inclusions might have originated from various sources, such as the raw materials, the manufacturing process, or environmental contamination and can greatly impact material properties by acting as stress concentrators, which may initiate cracks and reduce the overall strength and durability.

EDX point analysis was conducted on three distinct inclusions observed on the sample's surface as well as other points and regions of the steel matrix. A total of ten distinct locations were examined for clarity and comprehensive understanding of the sample's elemental composition. The analysis was systematically divided into two parts: point analysis and region analysis. The first seven locations, designated as points 1 through 7, were analyzed at specific points to determine the elemental composition at those precise

locations. The remaining three locations, labeled as regions 8 through 10, involved broader region analyses to capture the overall elemental distribution within larger areas of the sample. The analysis revealed a high count of sulfur and manganese (Table 4) at all the examined inclusion particles (points 1–3), as given in Figure 9. This suggests that the particles are likely MnS slag, which typically form during the processing of the steel.

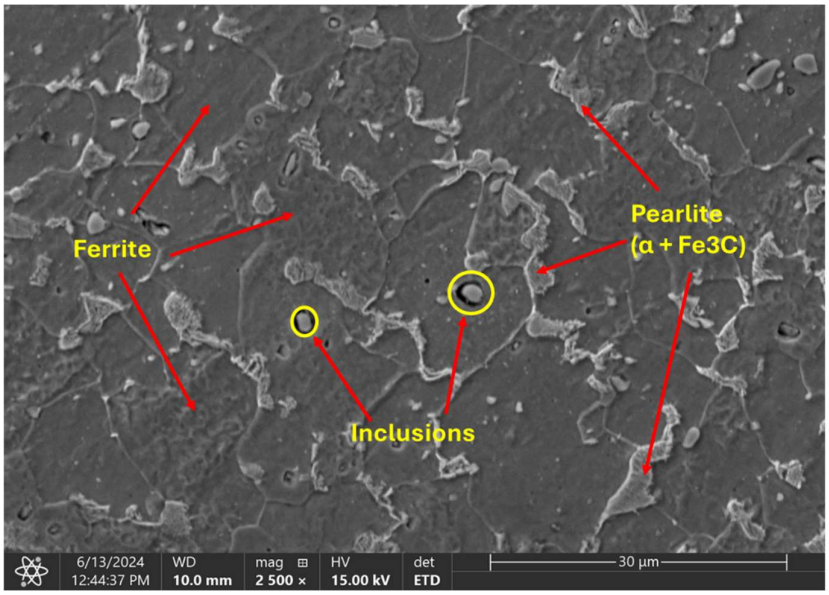

Figure 8. SEM of the microstructural characteristics of the cold-finished mild steel.

Table 4. Summary of weight % for points analysis on observed inclusions on sample's surface.

	Weight %		
Element	**Point 1**	**Point 2**	**Point 3**
C	12.6	11.7	13.5
Si	0.5	0.3	0.2
S	27.7	26.8	23.2
Mn	51.5	50.4	44.4
Fe	7.7	10.8	18.7

The thorough examination of the general material surface revealed that the matrix is composed of ferrite with some pearlite (Table 5), a microstructural feature consisting of alternating layers of soft and ductile ferrite (α-iron) and brittle and hard cementite (Fe_3C), whose combination give good strength and toughness situated at the ferrite grain boundaries.

Table 5. Weight % of EDX analysis on ferrite matrix.

	Weight %						
Element	**Point 4**	**Point 5**	**Point 6**	**Point 7**	**Region 8**	**Region 9**	**Region 10**
C	6.7	9.2	5.6	17.0	5.7	0.0	5.9
Al	0.0	0.0	0.0	0.0	0.0	0.0	0.0
Si	0.1	0.2	0.3	0.2	0.1	0.2	0.2
S	0.0	0.1	0.6	0.1	0.1	0.0	0.1
Mn	0.8	0.9	0.9	1.0	0.7	0.6	0.7
Fe	92.4	89.6	92.6	81.7	93.4	99.2	93.1

In the EDX analysis, points 4 to 7 at the grain boundaries exhibited a relatively higher carbon content and reduced ferrite, suggesting the presence of the pearlite phase. In

contrast, the regions (8 to 10) analyzed within the grains showed a high content of ferrite, indicating that the grains are primarily composed of ferrite.

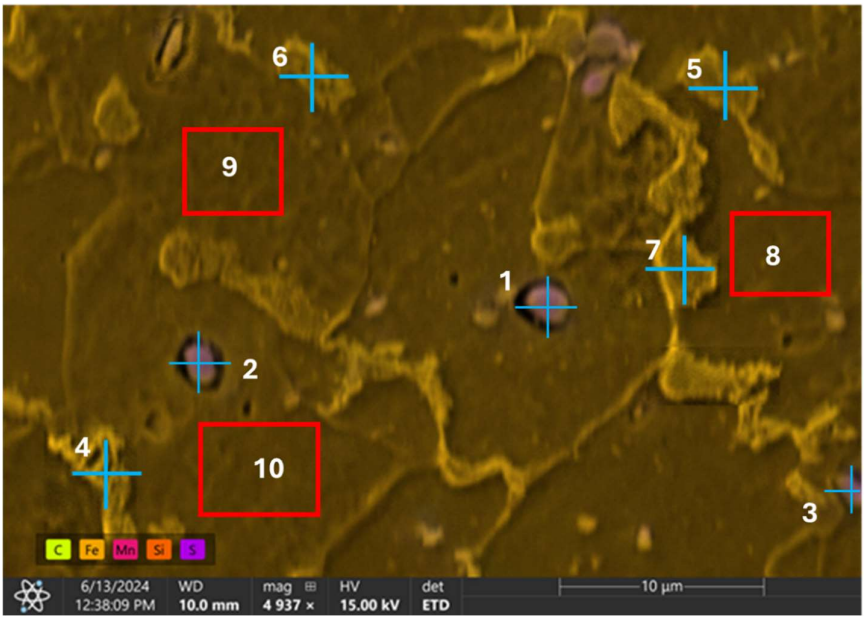

Figure 9. Energy dispersive X-ray spectroscopy analysis of observed inclusions and steel matrix.

The dominance of ferrite in the material further confirms the results obtained from the XRD analysis.

3.2. Fatigue Response to Varying Hydrogenating Conditions

Based on the findings of this study, the behavior of test samples under different hydrogenating conditions revealed an elaborate relationship between hydrogen permeation and the material's fatigue life. Initially, as hydrogen permeation increases, the number of cycles to failure decreases, indicating a reduction in the material's resistance to cyclic loading. However, at higher hydrogen contents, the reverse occurred, as the number of cycles to failure began to increase, as shown in Figure 10.

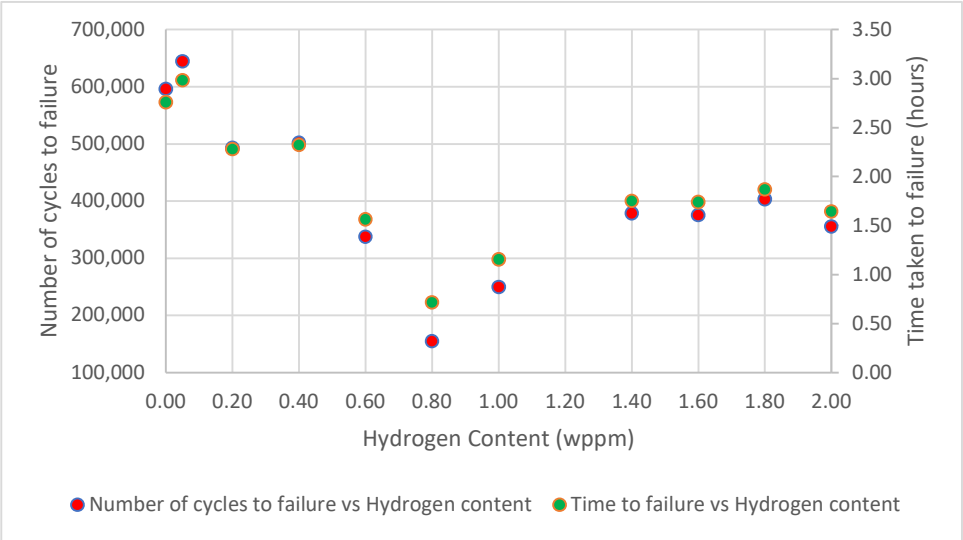

Figure 10. Graphical relationship between number of cycles to failure/time taken to fracture vs. hydrogen content.

In general, when hydrogen atoms diffuse into the steel lattice and defect sites, such as grain boundaries, vacancies, interstitials, and dislocations, they interact with their surroundings and cause significant change in the mechanical properties of the steel. The variation in the number of cycles to failure of mild steel under different hydrogenating conditions can be explained by considering the mechanistic effects of HE, HEDE [2,39], and HELP [16,17] on the material; as a result, the number of cycles to failure decreases and increases, as observed at varying hydrogen contents.

At a low to moderate hydrogen concentration, ranging from 0.05 to 0.80 wppm, as the hydrogen content increases, the fatigue life drops (Figure 10). This behavior can be attributed to a phenomenon termed HEDE, a mechanism that significantly contributes to the reduction in the fatigue life of hydrogen-charged mild steel samples. This phenomenon occurs due to the presence of hydrogen atoms within the steel's microstructure, which weakens the bonds between atoms and grains, leading to premature failure.

Previous research indicates that HEDE becomes more pronounced at high hydrogen concentrations, particularly when reaching levels that affect a material's mechanical properties; thus, it is more dependent on the extent to which dissolved hydrogen affects a material's mechanical properties than the quantity of hydrogen dissolved. In this context, the term "low to moderate" hydrogen concentrations refers to the levels of hydrogen relative to higher hydrogenating conditions. This classification does not specifically describe HEDE at low hydrogen levels, but rather indicates that the effects are observed at higher concentrations compared to uncharged samples.

Exposure of mild steel samples to hydrogen through electrochemical hydrogen charging causes hydrogen atoms to diffuse into the steel's microstructure. Atomic diffusion in a BCC lattice primarily occurs through interstitial hopping (diffusion), where atoms move from one tetrahedral site to another. However, absorbed hydrogen atoms tend to localize and remain trapped within microstructural defects, such as dislocations, vacancies, or grain boundaries, rather than freely diffusing through the lattice. These defects act as trapping sites, capturing hydrogen atoms and reducing their mobility. This dual behavior—interstitial diffusion combined with defect trapping—plays a crucial role in influencing the material's properties, particularly in environments where hydrogen embrittlement is a concern. Once inside the steel, hydrogen atoms tend to localize at regions of high stress and strain concentration, such as grain boundaries, crack tips, and other microstructural imperfections. The presence of hydrogen atoms at these locations weakens the metallic bonds between iron atoms by reducing the cohesive strength of the material. This weakening occurs for the reason that hydrogen atoms create additional tensile stress [29,40] within the lattice structure, making it easier for bonds to break under applied stress. The weakened bonds due to hydrogen atoms make the material more prone to crack initiation. Under cyclic loading conditions, as experienced during fatigue testing, these weakened regions are more likely to develop micro-cracks. The presence of hydrogen accelerates the formation of these cracks, reducing the number of cycles required for crack initiation.

Once a crack is initiated, the hydrogen atoms continue to assist in the propagation of the crack by further weakening the bonds at the crack tip. This process, known as hydrogen-enhanced crack growth [41,42], leads to faster crack propagation rates compared to hydrogen-free conditions. The reduction in cohesive strength at the crack tip allows the crack to grow with lower applied stress, thereby accelerating the overall failure process. The combined effect of accelerated crack initiation and faster crack propagation due to HEDE results in a significant reduction in the fatigue life of the hydrogen-charged samples. The material fails after fewer cycles of loading compared to samples not exposed to hydrogen, indicating a reduction in fatigue resistance.

At higher hydrogen concentrations, i.e., 0.80 to 2.00 wppm, HELP takes over. Through HELP mechanism, hydrogen facilitates dislocations motion within the crystal lattice by reducing the interaction energy and resistance from the lattice and other obstacles. Hence, the diffused hydrogen atoms cause localized plastic deformation. As dislocations move more easily in the presence of hydrogen, they can concentrate in specific regions rather than

being uniformly distributed throughout the material. The enhanced dislocation mobility leads to localized areas of intense plastic deformation, as dislocations tend to accumulate and move along specific paths where the barriers are lowest, creating regions of high strain. This implies that instead of the stress being distributed evenly throughout the material, it becomes concentrated in specific areas where dislocations are more mobile [43,44]. This deformation leads to improved toughness and ductility, hence, the increased HE resistance and enhanced fatigue life of the steel.

Also, the enhanced plasticity at high hydrogen concentrations can actually benefit the material's fatigue resistance in specific ways, including crack blunting, where the tips of growing cracks become more rounded and less sharp reducing the stress concentration at the crack tip and temporarily slowing down crack propagation. Also, the temporal increased plastic deformation allows for better redistribution of stress around the crack tip, potentially resulting in a slower rate of crack growth.

Furthermore, at high hydrogen concentrations, the material's response to cyclic loading may change such that the localized plastic deformation induced by hydrogen helps to absorb and dissipate some of the applied stress. This localized deformation can create zones such as microstructural deformation zones that are more resistant to further crack propagation, thereby extending the number of cycles to failure. In microstructural deformation zones, high hydrogen concentrations can cause localized deformation bands or shear bands to form [45,46]. These bands can absorb and dissipate applied stress more effectively than the surrounding material, which can help to limit crack growth.

Similarly, as shown in Figure 10, the plot of time to failure versus hydrogen concentration closely parallels the plot showing the number of cycles to failure as a function of hydrogen concentration. This similarity arises because, under constant load and frequency, the number of cycles to failure and time to failure are directly proportional, making these plots essentially identical.

3.3. Analysis of Fracture Surfaces

3.3.1. Uncharged Specimen

Fracture surface analysis of the uncharged (0.00 wppm) sample under a scanning electron microscope revealed a dimpled surface with few microcracks and microvoids, as shown in Figure 11.

Observed wrinkles (Figure 11a) on the specimen's surface near the fractured cross-section appeared as wavy, undulating patterns, resembling a crumpled sheet of paper. These wrinkles develop perpendicular to the direction of crack growth due to localized plastic deformation, which occurs unevenly because of microstructural inhomogeneities, stress concentrations, or variations in material properties. As the crack propagates under cyclic loading, repeated small-scale plastic deformations accumulate at the crack tip and along the fracture surface, leading to these wavy patterns. Their presence indicates that the material was ductile, absorbing and redistributing cyclic stresses before ultimately failing.

Ratchet marks (Figure 11b) are distinctive, linear features that appear as sharp steps on the fracture surface. These marks typically run parallel to the crack propagation direction and can be seen as boundaries separating different regions of the fracture surface. They form when multiple cracks, often originating from different stress concentrators (such as surface defects, inclusions, or notches), grow towards each other during cyclic loading. As these cracks propagate and merge, they create distinct steps or ridges where the fracture surfaces meet. The difference in crack front levels between the merging cracks creates a step-like feature. This mismatch is due to slight differences in crack growth rates, angles, or the material's response to cyclic loading at each initiation site.

The fatigue crack initiation zone (Figure 11c), often the smallest and most critical part of the fatigue fracture surface, is where the initial crack begins to form under cyclic loading. This zone can originate from a single point or multiple points within the material, particularly in areas where stress is highly concentrated. Such regions often exhibit microscopic roughness or small surface irregularities, which serve as the initial sites for

crack formation. Within this zone, visibly small microcracks can often be observed. These microcracks typically develop at stress concentrators such as surface scratches, inclusions, notches, pits, second-phase particles, and grain boundaries, and other microstructural inhomogeneities within the material act as focal points for the initiation of fatigue failure.

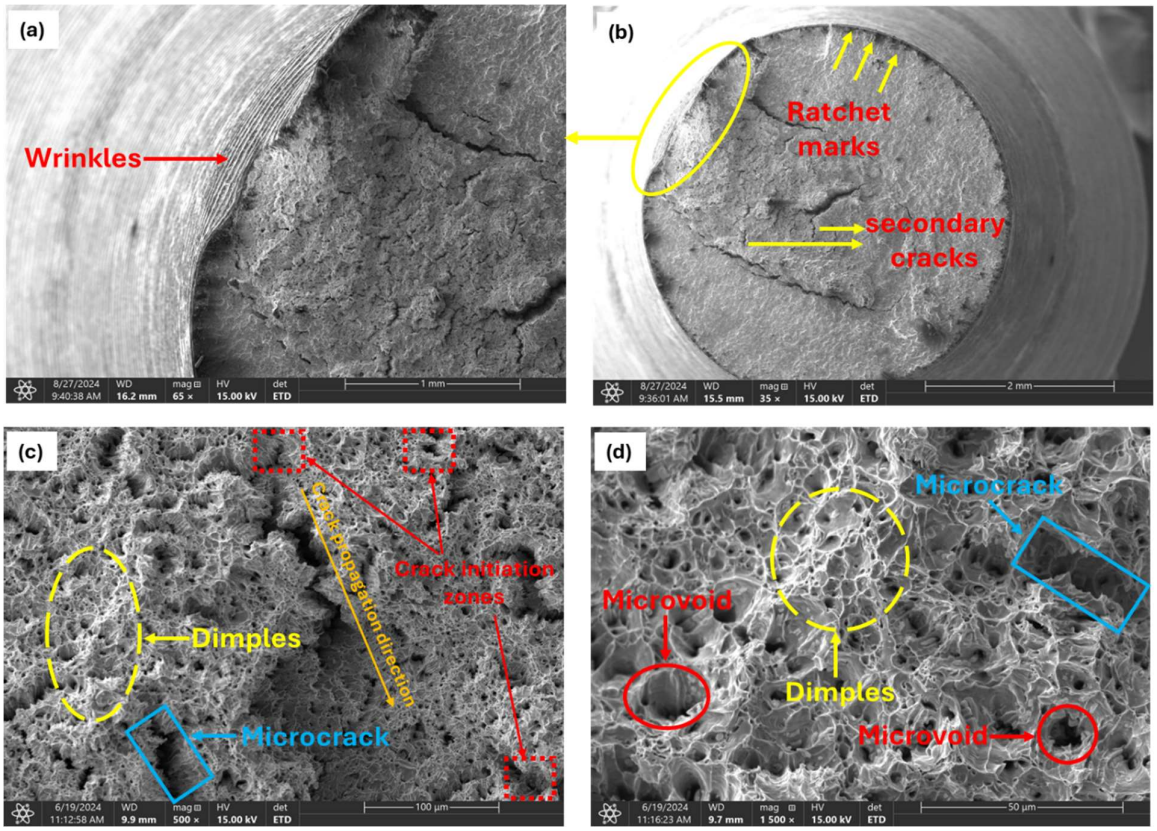

Figure 11. Fractographs of uncharged specimen showing ductile fracture characteristics. (**a**) Magnification of circled area in (**b**). (**b**) Low magnified (35X) view of fracture surface. (**c**) Magnified view (500X) of observed crack region in (**b**). (**d**) Magnified view of dimpled area in (**c**) (1500X).

These stress concentrators significantly reduce the fatigue strength of the material by providing an easy path for crack initiation and growth. The initiation zone represents the earliest stage of fatigue crack development, with the crack propagation typically radiating outward from this origin point. The direction of crack growth (Figure 11c) is often discernible through the orientation of microcracks and surface features.

During cyclic loading the said stress concentration sites are also favorable for the nucleation of microvoids. Dislocations pile up around these particles and inclusions, generating high local stresses that promote microvoid nucleation (Figure 11d). As cyclic loading continues, these nucleated microvoids begin to grow due to the applied cyclic stress causing plastic deformation around the voids. This plastic deformation leads to the expansion of microvoids, which eventually grow and coalesce with neighboring voids. The coalescence of these microvoids forms larger voids, reducing the effective load-bearing area of the material. Coalesced microvoids result in the formation of a characteristic dimpled pattern (Figure 11c,d) on the fracture surface. Each dimple corresponds to the site of a microvoid that has grown and merged with others. When a critical density of microvoids is reached, the remaining unfractured ligament of material between the voids can no longer sustain the applied stress. This leads to the rapid propagation of the crack through the remaining material.

The final rupture occurs in a ductile manner, characterized by extensive plastic deformation and energy absorption. This process leads to the formation of the observed dimpled

fracture surface, appearing as rounded, crater-like depressions. The size and distribution of these dimples enable comprehension of the nature of the material and the conditions under which it failed. Larger dimples typically indicate sites where larger inclusions or second-phase particles were present, while smaller dimples indicate more homogeneous regions of the material.

3.3.2. Moderately Charged Samples

The analysis of fractured surfaces of samples charged with relatively lower hydrogen contents (i.e., 0.05, 0.20, 0.40 wppm) revealed a combination of ductile and brittle fatigue features (Figure 12). This phenomenon can be explained by the interaction between hydrogen embrittlement mechanisms and the inherent properties of the material. At lower hydrogen charging levels, the distribution of hydrogen within the material may be uneven. As a result, regions with higher hydrogen concentrations exhibit more brittle behavior, while other areas retain the material's inherent ductility.

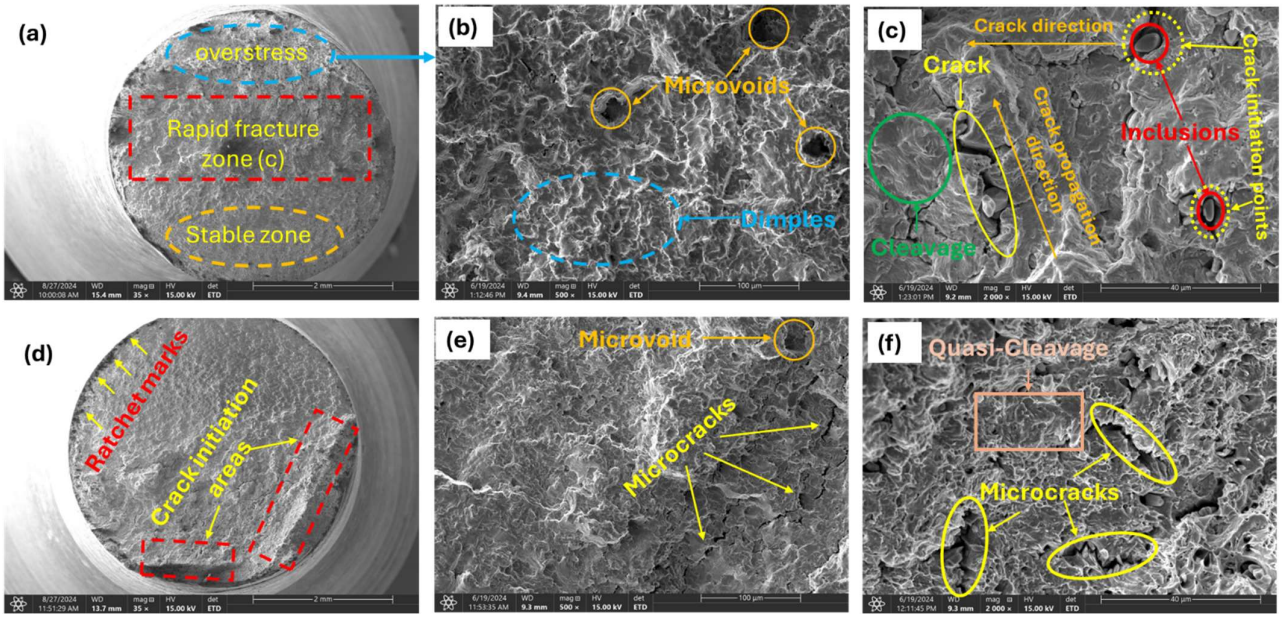

Figure 12. Fracture surfaces of low hydrogenated samples; (**a**) 0.05 wppm charged specimen at low magnification (35×); (**b**) magnified view of overstress zone in (**a**) 500×; (**c**) rapid fracture zone in (**a**) 2000×; (**d**) low magnification view of 0.20 wppm (35×); observed features of crack initiation areas in (**d**) at higher magnifications (**e**) 500×; (**f**) 2000×.

The overstress zone (Figure 12a) formed after the specimen experienced progressive crack growth due to cyclic loading. This zone is where the remaining material can no longer support the load, leading to sudden failure. Typically, the material in this region undergoes rapid plastic deformation, characteristic of ductile fracture, which results in features such as tearing, microvoid coalescence, and dimpling, as shown in Figure 12b.

The rapid fracture zone (Figure 12a) is typically brittle. It occurs when the crack grows to a critical size and the remaining material can no longer withstand the applied load. The fracture occurs suddenly and often without significant plastic deformation. As a result, the surface in this area tends to exhibit features characteristic of a brittle fracture, such as a smooth, shiny appearance, cleavage facets, and microcracks (Figure 12c). These features indicate that the material broke with little to no plasticity, which is typical of brittle behavior.

These brittle features (Figure 12c,f) observed on the fracture surfaces of hydrogen-charged materials are directly linked to the HEDE mechanism as mentioned above in Section 3.2. Hydrogen atoms adsorb and diffuse into the material, accumulating at stress concentration sites such as grain boundaries or dislocation cores. This accumulation of

hydrogen reduces the cohesive strength of atomic bonds within the material, making it easier for these bonds to break under stress. The weakened cohesive strength causes the separation of atomic planes at stresses lower than would be required in the absence of hydrogen.

The presence of hydrogen atoms particularly weakens atomic bonds at grain boundaries and other defects, leading to the initiation of microcracks. These microcracks can rapidly grow and coalesce, forming larger cracks. The weakened bonds also cause cracks to propagate along specific crystallographic planes, resulting in the appearance of cleavage facets on the fracture surface. The combination of cleavage facets and microcracks indicates a brittle fracture mode, driven by the HEDE mechanism. This results in the material fracturing with minimal plastic deformation, exhibiting pronounced brittle behavior. Additionally, brittle fractures can manifest as transgranular cracks, where the crack propagates through the grains rather than along the grain boundaries.

Contrarywise, in areas less affected by hydrogen diffusion, the fatigue fracture surface exhibits ductile topographies (Figure 12b), as discussed in Section 3.3.1. Observed crack initiation points and propagation directions are as explained above.

3.3.3. Highly Charged Samples

For samples charged with comparatively higher hydrogen contents (1.60, 1.80, and 2.00 wppm), analysis of the fracture surfaces exhibited distinct features that differ significantly from those observed in uncharged and moderately charged samples.

The overstress zone (Figure 13a,b) in brittle fatigue failure is marked by a sudden, rapid fracture, signaling the shift from stable crack growth to abrupt, brittle failure. This zone typically features a clean break with characteristics such as cleavage facets or a mirror-like surface, indicative of brittle behavior. Initially, a fatigue crack forms and propagates incrementally under cyclic loading. In brittle materials, the crack grows progressively with a smooth, flat surface and minimal plastic deformation. As the crack advances, stress concentrations around the crack tip increase, leading to the formation of additional microcracks or further crack growth. When the crack reaches a critical size, the remaining material can no longer withstand the applied load, resulting in sudden, catastrophic failure. This failure occurs rapidly without significant plastic deformation.

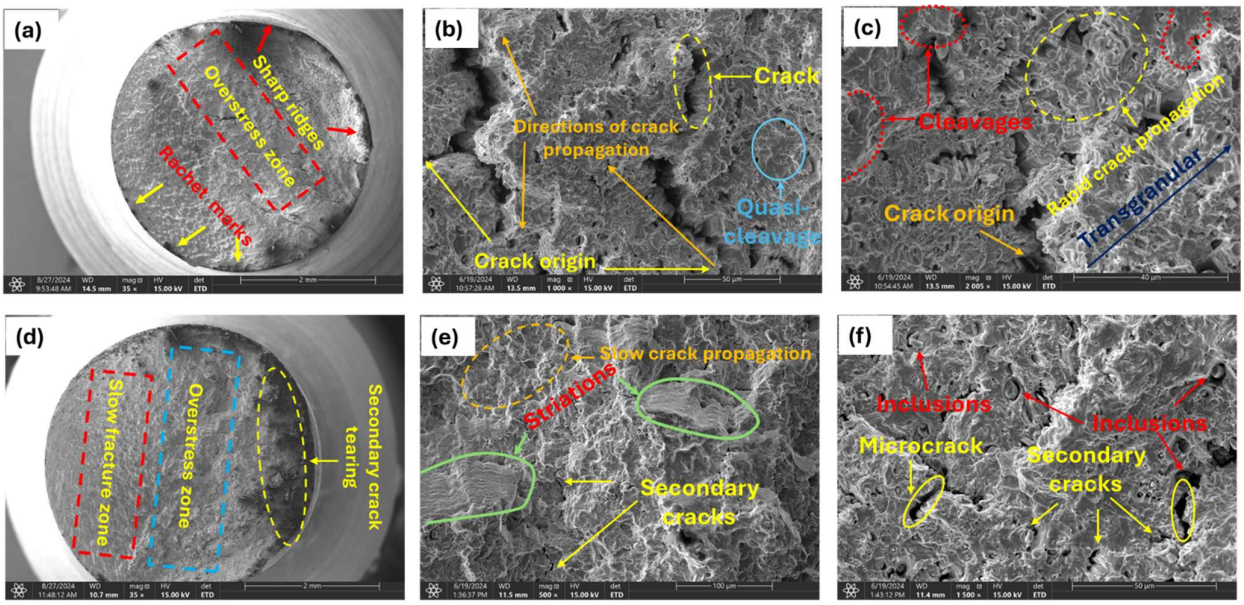

Figure 13. Micrograph of highly charged specimens; (**a**) 2.0 wppm specimen (35×); overstress zone of 2.0 wppm at high magnifications (**b**) (1000×); (**c**) 2005×; (**d**) 1.80 wppm charged specimen (35×); magnified view of the slow fracture zone of 1.80 wppm charged specimen (**e**) (500×); (**f**) 1500×.

The observation of cleavage facets, macrocracks, secondary cracks, and striations (Figure 13c,e,f) in highly hydrogen-charged materials can be attributed to the HELP mechanism. Hydrogen atoms enhance dislocation mobility, leading to localized plastic deformation (i.e., work-hardening) that concentrates stress, facilitates crack initiation and propagation, and results in the dense fracture surface features observed. Hydrogen atoms diffuse into the material and accumulate at dislocation cores and grain boundaries, reducing the energy barrier for dislocation motion. This leads to increased dislocation activity and localized plastic deformation, creating regions of high internal stress, particularly at dislocation pileups. These high-stress regions initiate cracks more easily due to the presence of hydrogen, which weakens atomic bonds. Cracks propagate along cleavage planes where atomic bonds are weaker, facilitated by the presence of hydrogen. The rapid propagation of cracks along these planes results in the formation of cleavage facets (Figure 13c) on the fracture surface, indicating a brittle fracture mode. The presence of hydrogen accelerates the fatigue crack growth rate and enhances the brittleness of the material, making cleavage the dominant fracture mode under the given experimental conditions.

Observed striations (Figure 13e) are indicative of incremental crack growth under cyclic loading. They appear as fine, parallel lines perpendicular to the direction of crack propagation. In the context of HE and HELP, striations form due to repeated cycles of localized plastic deformation and crack advancement. Hydrogen enhances the mobility of dislocations, leading to cyclic plastic deformation at the crack tip. Under fatigue loading, samples also experience repeated application and removal of stress, which leads to the initiation and propagation of fatigue cracks. Each cycle of loading causes a small, incremental advancement of the crack front whose growth rate is accelerated by the presence of diffused hydrogen. Hydrogen enhances the ease with which cracks initiate by weakening the metal at the crack tip. The crack propagates in a stepwise pattern with each load cycle, leaving behind striations on the fracture surface. Each striation corresponds to one complete load cycle. The presence of diffused hydrogen makes striations more prominent due to the increased crack growth rate and more brittle nature of the fracture process.

Additionally, high-stress regions resulting from dislocation pileups through the HELP mechanism initiate microcracks more easily at stress concentrators such as surface imperfections, inclusions (Figure 13f), or grain boundaries due to the presence of hydrogen, which weakens atomic bonds. Under applied external stress, such as cyclic loading, microcracks propagate and coalesce, with hydrogen reducing resistance to crack growth. This coalescence reduces the effective load-bearing cross-section of the material, increasing the local stress further. Under continued cyclic loading, these coalesced cracks propagate in a brittle manner, often along specific crystallographic planes or grain boundaries. Once the microcracks have coalesced sufficiently, they form a dominant macrocrack that propagates through the material as shown in Figure 13b above. This macrocrack grows with each loading cycle, driven by the high stress intensity at its tip. The macrocrack grows to a critical size where the remaining cross-sectional area can no longer support the applied load, leading to sudden catastrophic failure. The formation of macrocracks causes stress redistribution, creating new regions of high stress around the main crack. These new high-stress regions initiate secondary cracks due to localized plasticity and weakened atomic bonds. Secondary cracks propagate and contribute to the overall fracture.

The crack propagates through the grains in a brittle manner, often leaving behind steps or ledges. The surface shows sharp, stepped features that indicate a brittle transgranular fracture (Figure 13c), with no evidence of plastic deformation. As already mentioned above, reduction in bond strength makes it easier for cracks to propagate through the grains rather than along the grain boundaries. Also, in instances where grains contain trapping sites for hydrogen such as voids, the cracks propagate transgranularly, as grains themselves are embrittled by hydrogen.

Slow and rapid crack propagation zones were observed on the fracture surface [47–49]. The fracture surface in the fast propagation zone (Figure 13c) appeared smoother compared to the slow zone. Here, the crack propagated more rapidly, with less interaction with

the microstructure, resulting in a smoother surface. This smoothness is indicative of the material failing in a more brittle manner due to the high crack growth rate. The fast propagation zone typically occurs when the stress intensity factor approaches the material's fracture toughness, leading to rapid and unstable crack growth. This zone is usually associated with the final stages of fatigue failure, where the remaining cross-sectional area can no longer sustain the applied load, ultimately resulting in catastrophic failure.

In contrast, in the slow crack propagation zone (Figure 13d,e), the surface appeared rough and granular, a result of the crack interacting with the material's microstructure. This granularity occurred as the crack encountered various microstructural features, such as grains, precipitates, or inclusions, which caused deflection and branching of the crack path. Small, step-like features were also present, indicating the crack's advancement through different planes within the material. This zone is characteristic of a relatively low stress intensity and a steady, controlled crack growth rate.

EDX analysis was conducted at three distinct points on the inclusions observed on the fracture surface of the 1.80 wppm charged sample, as illustrated in Figure 13f, to determine the elemental composition at these locations. Analyzed points are highlighted in Figure 14 below with the overall outcome in Table 6.

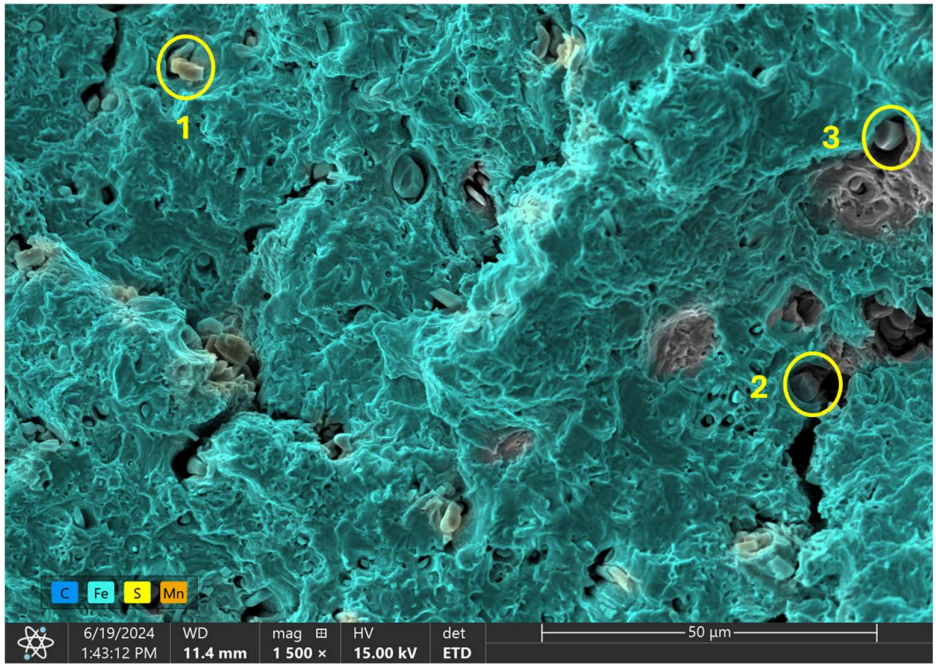

Figure 14. EDX analysis of observed inclusion phases on 1.80 wppm charged sample.

Table 6. Summary of elemental weight% on inclusions on 1.8 wppm charged sample.

	Weight %		
Element	**Point 1**	**Point 2**	**Point 3**
C	10.6	1.9	2.5
F	0.0	0.0	0.0
S	52.5	2.3	0.6
Mn	29.9	69.8	31.2
Fe	7.0	25.9	65.7
Si	0.0	0.1	0.0

The EDX spectrum at the first point exhibited the highest count for sulfur (S). This significant presence of sulfur indicates that the inclusion at this location is likely sulfide-based. Sulfide inclusions are common in steel and can form compounds such as manganese sulfide (MnS) or iron sulfide (FeS). The high sulfur content suggests the presence of MnS or

FeS inclusions, which are known to affect the material's fracture behavior and mechanical performance.

At the second point, the EDX analysis showed the highest count for manganese (Mn). The elevated manganese content, when considered alongside the sulfur detected at point 1, further supports the possible presence of manganese sulfide (MnS) inclusions. Manganese sulfide inclusions are typical in steel and can have a notable impact on its mechanical properties, particularly its ductility and toughness. The detection of high manganese levels at this point confirms the likelihood of MnS inclusions contributing to the observed fracture characteristics.

The EDX spectrum at the third point revealed the highest count for iron (Fe). This suggests that the region of the inclusion at this point has a higher concentration of iron. The high iron content may imply a transition zone from the inclusion to the surrounding steel matrix or the presence of iron-rich phases within the inclusion itself. This transition could signify the interaction between the inclusion and the steel matrix, which can influence the fracture mechanics and overall structural integrity of the material.

Observed inclusions can serve as decohesion sites in metals under fatigue loading through several mechanisms, including stress concentration, interface weakness, microstructural discontinuities, plastic incompatibility, and crack initiation and propagation. These mechanisms collectively contribute to the initiation and growth of fatigue cracks, ultimately leading to the fracture of the metal.

Due to the mismatch in mechanical properties between the inclusion and the surrounding metal, applied stress is not uniformly distributed, creating localized stress concentrations in the metal matrix. The stress concentration factor (SCF) around the inclusion can be significantly higher than the applied stress, leading to localized plastic deformation and initiation of microcracks at the inclusion–matrix interface. The interface between an inclusion and the metal matrix is often weaker than the matrix itself due to reduced bonding or differences in thermal expansion coefficients, leading to residual stresses during cooling from processing temperatures. Under cyclic loading, these weak interfaces can decohere, initiating cracks that propagate under continued fatigue loading.

Inclusions can also act as microstructural discontinuities within the material, which disrupts the continuity of the metal's grain structure, creating sites where crack initiation is more probable. The plastic deformation behavior of inclusions is often different from that of the metal matrix. When the metal undergoes cyclic loading, the difference in plasticity between the inclusion and the matrix leads to localized strain incompatibility. This incompatibility generates additional stress concentrations, which can initiate microcracks at or near the inclusion.

4. Conclusions

In this study, the fatigue behavior of cold-finished mild steel under varying cathodic hydrogen charging conditions was investigated to understand the material's performance and susceptibility to hydrogen embrittlement. The findings revealed significant discovery into how hydrogen permeation affects fatigue life and crack propagation mechanisms. It was found from this study that:

1. The number of cycles to failure initially decreased with increasing hydrogen concentration, dropping from 596,057 cycles for uncharged samples (0.00 wppm) to 154,925 cycles at an intermediate hydrogen concentration (0.80 wppm). This decline highlights the detrimental impact of hydrogen embrittlement, which accelerates fatigue crack initiation and propagation.
2. Interestingly, at very high hydrogen concentrations, the number of cycles to failure showed an astonishing increase of 249,775 for 1.00 wppm through to 355,407 for 2.00 wppm.
3. There is a suggestive presence of a threshold beyond which additional hydrogen may alter the dominant fatigue mechanisms, possibly due to changes in crack propagation

behavior or the saturation of hydrogen-related defects and mechanisms such as HELP and HEDE.

4. The fatigue failure behavior of the tested samples revealed a clear correlation between the hydrogen concentration and fracture characteristics. Uncharged samples exhibited predominantly ductile failure modes, characterized by microvoid coalescence and dimpling, which are indicative of the material's inherent toughness. In contrast, samples with low hydrogen concentrations (0.05, 0.20, and 0.40 wppm) displayed a mixture of ductile and brittle features, suggesting partial hydrogen diffusion. This selective embrittlement affected certain regions of the microstructure, while other areas retained their original ductility. Highly charged samples (1.60, 1.80, and 2.00 wpmm), however, exhibited pronounced brittle fracture characteristics, including cleavage facets, sharp ridges, and the formation of microcracks. These observations emphasize the detrimental impact of elevated hydrogen concentrations on the material.

Author Contributions: Conceptualization, Z.N.F.; methodology, E.S. and Z.N.F.; formal analysis, E.S. and Z.N.F.; investigation, E.S. and Z.N.F.; resources, E.S. and Z.N.F.; writing—original draft preparation, E.S.; writing—review and editing, E.S. and Z.N.F.; supervision, Z.N.F.; project administration, Z.N.F.; funding acquisition, Z.N.F. All authors have read and agreed to the published version of the manuscript.

Funding: This research was funded by the Natural Sciences and Engineering Research Council of Canada (NSERC), grant number RGPIN 05125-17.

Data Availability Statement: The original contributions presented in the study are included in the article; further inquiries can be directed to the corresponding author.

Conflicts of Interest: The authors declare no conflicts of interest.

References

1. Nagao, A.; Dadfarnia, M.; Somerday, B.P.; Sofronis, P.; Ritchie, R.O. Hydrogen-Enhanced-Plasticity Mediated Decohesion for Hydrogen-Induced Intergranular and "Quasi-Cleavage" Fracture of Lath Martensitic Steels. *J. Mech. Phys. Solids* **2018**, *112*, 403–430. [CrossRef]
2. Troiano, A.R. The Role of Hydrogen and Other Interstitials in the Mechanical Behavior of Metals. *Metallogr. Microstruct. Anal.* **2016**, *5*, 557–569. [CrossRef]
3. Li, X.; Liu, C.; Wang, X.; Dai, Y.; Zhan, M.; Liu, Y.; Yang, K.; He, C.; Wang, Q. Effect of Microstructure on Small Fatigue Crack Initiation and Early Propagation Behavior in Super Austenitic Stainless Steel 654SMO. *Int. J. Fatigue* **2024**, *179*, 108022. [CrossRef]
4. Brem, J.C.; Barlat, F.; Dick, R.E.; Yoon, J.-W. *Characterizations of Aluminum Alloy Sheet Materials Numisheet 2005*; American Institute of Physics: College Park, ML, USA, 2005; Volume 778.
5. Xue, Y.; Solanki, K.; Steele, G.; Horstemeyer, M.; Newman, J. Quantitative Uncertainty Analysis for a Mechanistic Multistage Fatigue Model. In Proceedings of the 48th AIAA/ASME/ASCE/AHS/ASC Structures, Structural Dynamics, and Materials Conference, Honolulu, HI, USA, 23–26 April 2007; American Institute of Aeronautics and Astronautics: Reston, VA, USA, 2012. [CrossRef]
6. Park, J.Y.; Park, Y.C.; Kim, H.-K. A Methodology for Fatigue Reliability Assessment Considering Stress Range Distribution Truncation. *Int. J. Steel Struct.* **2018**, *18*, 1242–1251. [CrossRef]
7. Huffman, P.J.; Correia, J.A.F.O.; Mourão, A.; Bittencourt, T.; Calçada, R. Predicted Distribution in Measured Fatigue Life from Expected Distribution in Cyclic Stress–Strain Properties Using a Strain-Energy Based Damage Model. In *Structural Integrity and Fatigue Failure Analysis*; Lesiuk, G., Szata, M., Blazejewski, W., de Jesus, A.M.P., Correia, J.A.F.O., Eds.; Springer International Publishing: Cham, Switzerland, 2022; pp. 65–71.
8. Koster, M.; Lis, A.; Lee, W.J.; Kenel, C.; Leinenbach, C. Influence of Elastic–Plastic Base Material Properties on the Fatigue and Cyclic Deformation Behavior of Brazed Steel Joints. *Int. J. Fatigue* **2016**, *82*, 49–59. [CrossRef]
9. Čanžar, P.; Tonković, Z.; Kodvanj, J. Microstructure Influence on Fatigue Behaviour of Nodular Cast Iron. *Mater. Sci. Eng. A* **2012**, *556*, 88–99. [CrossRef]
10. Ponson, L.; Bonamy, D. Crack Propagation in Brittle Heterogeneous Solids: Material Disorder and Crack Dynamics. In *IUTAM Symposium on Dynamic Fracture and Fragmentation*; Ravi-Chandar, K., Vogler, T.J., Eds.; Springer: Dordrecht, The Netherlands, 2010; pp. 21–31.
11. Song, S.W.; Kwon, Y.J.; Lee, T.; Lee, C.S. Effect of Al Addition on Low-Cycle Fatigue Properties of Hydrogen-Charged High-Mn TWIP Steels. *Mater. Sci. Eng. A* **2016**, *677*, 421–430. [CrossRef]
12. Chen, X.; Ma, L.; Xie, H.; Zhao, F.; Ye, Y.; Zhang, L. Effects of External Hydrogen on Hydrogen-Assisted Crack Initiation in Type 304 Stainless Steel. *Anti-Corros Methods Mater.* **2020**, *67*, 331–335. [CrossRef]

13. Pal, S.; Singh Raman, R.K. Determination of Threshold Stress Intensity Factor for Stress Corrosion Cracking (KISCC) of Steel Heat Affected Zone. *Corros. Sci.* **2009**, *51*, 2443–2449. [CrossRef]
14. De Pannemaecker, A.; Fouvry, S.; Brochu, M.; Buffiere, J.Y. Identification of the Fatigue Stress Intensity Factor Threshold for Different Load Ratios R: From Fretting Fatigue to C(T) Fatigue Experiments. *Int. J. Fatigue* **2016**, *82*, 211–225. [CrossRef]
15. Kitahara, G.; Asada, T.; Matsuoka, H. Effects of Diffusible Hydrogen on Fatigue Life of Spot Welds in High-Tensile-Strength Steel Sheets. *ISIJ Int.* **2023**, *63*, 889–898. [CrossRef]
16. Djukic, M.B.; Bakic, G.M.; Sijacki Zeravcic, V.; Sedmak, A.; Rajicic, B. The Synergistic Action and Interplay of Hydrogen Embrittlement Mechanisms in Steels and Iron: Localized Plasticity and Decohesion. *Eng. Fract. Mech.* **2019**, *216*, 106528. [CrossRef]
17. Örnek, C.; Şeşen, B.M.; Ürgen, M.K. Understanding Hydrogen-Induced Strain Localization in Super Duplex Stainless Steel Using Digital Image Correlation Technique. *Met. Mater. Int.* **2022**, *28*, 475–486. [CrossRef]
18. Neikter, M.; Colliander, M.; de Andrade Schwerz, C.; Hansson, T.; Åkerfeldt, P.; Pederson, R.; Antti, M.L. Fatigue Crack Growth of Electron Beam Melted TI-6AL-4V in High-Pressure Hydrogen. *Materials* **2020**, *13*, 1287. [CrossRef] [PubMed]
19. Beachem, C.D. A New Model for Hydrogen-Assisted Cracking (Hydrogen "Embrittlement"). *Metall. Mater. Trans. B* **1972**, *3*, 441–455. [CrossRef]
20. Lynch, S. Hydrogen Embrittlement Phenomena and Mechanisms. *Corros. Rev.* **2012**, *30*, 105–123. [CrossRef]
21. Oag-Bvg Independent Auditor's Report | 2022 Reports of the Commissioner of the Environment and Sustainable Development to the Parliament of Canada Hydrogen's Potential to Reduce Greenhouse Gas Emissions. 26 April 2022. Available online: https://www.oag-bvg.gc.ca/internet/English/parl_cesd_202204_03_e_44023.html (accessed on 1 September 2024).
22. Davis, M.; Okunlola, A.; Di Lullo, G.; Giwa, T.; Kumar, A. Greenhouse Gas Reduction Potential and Cost-Effectiveness of Economy-Wide Hydrogen-Natural Gas Blending for Energy End Uses. *Renew. Sustain. Energy Rev.* **2023**, *171*, 112962. [CrossRef]
23. Si, X.; Lu, R.; Zhao, Z.; Yang, X.; Wang, F.; Jiang, H.; Luo, X.; Wang, A.; Feng, Z.; Xu, J.; et al. Catalytic Production of Low-Carbon Footprint Sustainable Natural Gas. *Nat. Commun.* **2022**, *13*, 258. [CrossRef]
24. Sun, T.; Shrestha, E.; Hamburg, S.P.; Kupers, R.; Ocko, I.B. Climate Impacts of Hydrogen and Methane Emissions Can Considerably Reduce the Climate Benefits across Key Hydrogen Use Cases and Time Scales. *Environ. Sci. Technol.* **2023**, *58*, 5299–5309. [CrossRef]
25. *ASTM E3-11*; Standard Guide for Preparation of Metallographic Specimens1. American Society for Testing and Materials (ASTM) International: West Conshohocken, PA, USA, 2017. [CrossRef]
26. *ASTME407−23*; Standard Practice for Microetching Metals and Alloys1. American Society for Testing and Materials (ASTM) International: West Conshohocken, PA, USA, 2023. [CrossRef]
27. *ASTM D785-23*; Standard Test Method for Rockwell Hardness of Plastics and Electrical Insulating Materials. American Society for Testing and Materials (ASTM) International: West Conshohocken, PA, USA, 2023. [CrossRef]
28. *ASTM E18-20*; Standard Test Methods for Rockwell Hardness of Metallic Materials. American Society for Testing and Materials (ASTM) International: West Conshohocken, PA, USA, 2022. [CrossRef]
29. Sey, E.; Farhat, Z.N. Evaluating the Effect of Hydrogen on the Tensile Properties of Cold-Finished Mild Steel. *Crystals* **2024**, *14*, 529. [CrossRef]
30. Devanathan, M.; Stachurski, Z. The Adsorption and Diffusion of Electrolytic Hydrogen in Palladium. *Proc. R. Soc. Lond. Ser. A Math. Phys. Sci.* **1962**, *270*, 90–102. [CrossRef]
31. *ISO 17081*; Method of Measurement of Hydrogen Permeation and Determination of Hydrogen Uptake and Transport in Metals by an Electrochemical Technique. International Organization for Standardization: Geneva, Switzerland, 2014.
32. Li, Q.; Ghadiani, H.; Jalilvand, V.; Alam, T.; Farhat, Z.; Islam, M.A. Hydrogen Impact: A Review on Diffusibility, Embrittlement Mechanisms, and Characterization. *Materials* **2024**, *17*, 965. [CrossRef] [PubMed]
33. Röthig, M.; Hoschke, J.; Tapia, C.; Venezuela, J.; Atrens, A. A Review of Gas Phase Inhibition of Gaseous Hydrogen Embrittlement in Pipeline Steels. *Int. J. Hydrogen Energy* **2024**, *60*, 1239–1265. [CrossRef]
34. Iyer, R.N.; Pickering, H.W.; Zamanzadeh, M. Analysis of Hydrogen Evolution and Entry into Metals for the Discharge-Recombination Process. *J. Electrochem. Soc.* **1989**, *136*, 2463. [CrossRef]
35. Devanathan, M.; Stachurski, Z. The Mechanism of Hydrogen Evolution on Iron in Acid Solutions by Determination of Permeation Rates. *J. Electrochem. Soc.* **1964**, *111*, 619. Available online: https://ui.adsabs.harvard.edu/link_gateway/1964JElS..111..619D/doi:10.1149/1.2426195 (accessed on 1 September 2024). [CrossRef]
36. Lipski, A. Rapid Determination of the Wöhler's Curve for Aluminum Alloy 2024-T3 by Means of the Thermographic Method. *AIP Conf. Proc.* **2016**, *1780*, 020004.
37. Mlikota, M.; Schmauder, S.; Božić, Ž. Calculation of the Wöhler (S-N) Curve Using a Two-Scale Model. *Int. J. Fatigue* **2018**, *114*, 289–297. [CrossRef]
38. *ASTM A370*; Standard Test Methods and Definitions for Mechanical Testing of Steel Products. ASTM: West Conshohocken, PA, USA, 2024. [CrossRef]
39. Wasim, M.; Djukic, M.B.; Ngo, T.D. Influence of Hydrogen-Enhanced Plasticity and Decohesion Mechanisms of Hydrogen Embrittlement on the Fracture Resistance of Steel. *Eng. Fail. Anal.* **2021**, *123*, 105312. [CrossRef]
40. Shibata, A.; Yonemura, T.; Momotani, Y.; Park, M.; Takagi, S.; Madi, Y.; Besson, J.; Tsuji, N. Effects of Local Stress, Strain, and Hydrogen Content on Hydrogen-Related Fracture Behavior in Low-Carbon Martensitic Steel. *Acta. Mater.* **2021**, *210*, 116828. [CrossRef]

41. Matsunaga, H.; Takakuwa, O.; Yamabe, J.; Matsuoka, S. Hydrogen-Enhanced Fatigue Crack Growth in Steels and Its Frequency Dependence. *Philos. Trans. R. Soc. A* **2017**, *375*, 20160412. [CrossRef]
42. Traidia, A.; Chatzidouros, E.; Jouiad, M. Review of Hydrogen-Assisted Cracking Models for Application to Service Lifetime Prediction and Challenges in the Oil and Gas Industry. *Corros. Rev.* **2018**, *36*, 323–347. [CrossRef]
43. Polyanskiy, V.A.; Belyaev, A.K.; Sedova, Y.S.; Yakovlev, Y.A. Mesoeffect of the Dual Mechanism of Hydrogen-Induced Cracking. *Phys. Mesomech.* **2022**, *25*, 466–478. [CrossRef]
44. Gong, W.; Trtik, P.; Ma, F.; Jia, Y.; Li, J.; Bertsch, J. Hydrogen Diffusion and Precipitation under Non-Uniform Stress in Duplex Zirconium Nuclear Fuel Cladding Investigated by High-Resolution Neutron Imaging. *J. Nucl. Mater.* **2022**, *570*, 153971. [CrossRef]
45. Schaefer, F.; Geyer, S.; Motz, C. How Hydrogen Affects the Formation and Evolution of Persistent Slip Bands in High-Purity α-Iron. *Adv. Eng. Mater.* **2023**, *25*, 2201932. [CrossRef]
46. Sofronis, P.; Liang, Y.; Aravas, N. Hydrogen Induced Shear Localization of the Plastic Flow in Metals and Alloys. *Eur. J. Mech.-A/Solids* **2001**, *20*, 857–872. [CrossRef]
47. Jones, K.; Musinski, W.D.; Pilchak, A.L.; John, R.; Shade, P.A.; Rollett, A.D.; Holm, E.A. Predicting Fatigue Crack Growth Metrics from Fractographs: Towards Fractography by Computer Vision. *Int. J. Fatigue* **2023**, *177*, 107915. [CrossRef]
48. Chudnovsky, A. Slow Crack Growth, Its Modeling and Crack-Layer Approach: A Review. *Int. J. Eng. Sci.* **2014**, *83*, 6–41. [CrossRef]
49. Zhang, P.; Li, J.; Zhao, Y.; Li, J. Crack Propagation Analysis and Fatigue Life Assessment of High-Strength Bolts Based on Fracture Mechanics. *Sci. Rep.* **2023**, *13*, 14567. [CrossRef]